RSC Advances

ROYAL SOCIETY OF CHEMISTRY

www.rsc.org/advances

Nanocomposites of nitrogen-doped graphene decorated with a palladium silver bimetallic alloy for use as a biosensor for methotrexate detection

Hanieh Ghadimi[a,*], Bahman Nasiri–Tabrizi[b,*], Pooria Moozarm Nia[a], Wan Jefrey Basirun[a,c], Ramin M.A. Tehrani[d], Farnaz Lorestani[a]

[a]*Department of Chemistry, Faculty of Science, University of Malaya, 50603 Kuala Lumpur, Malaysia.*

[b]*Advanced Materials Research Center, Materials Engineering Department, Najafabad Branch, Islamic Azad University, Isfahan, Iran*

[c]*Institute of Nanotechnology and Catalysis (NanoCat), University Malaya, Kuala Lumpur 50603, Malaysia.*

[d]*Department of Chemistry, Yadegar-e- Imam Khomeini (RAH) Shahre Rey Branch, Islamic Azad University, Tehran, Iran*

*Corresponding authors: Department of Chemistry, University of Malaya, Kuala Lumpur 50603, Malaysia. Tel: +60379675330; fax: +60379675330. Advanced Materials Research Center, Materials Engineering Department, Najafabad Branch, Islamic Azad University, Isfahan, Iran. *Email addresses:* Hanieh.Ghadimi@yahoo.com, bahman_nasiri@hotmail.com

Abstract

The synthesis and application of composites of N–graphene decorated with a bimetallic palladium-silver alloy (PdAg/NG–GCE) for the detection of methotrexate (MTX) are described. The nanocomposites were synthesized with different ratios of Ag and Pd (3:1, 1:1 and 2:1). Energy dispersive X-ray spectroscopy (EDS) and X-ray diffraction (XRD) show that the Pd and Ag cations were completely reduced to Pd and Ag, respectively, during the formation of PdAg/NG. Transmission electron microscopy (TEM) showed a good loading between the PdAg alloy nanoparticles and the NG nanosheets with a Pd:Ag ratio of 1:1. The TEM results also depicted the existence of PdAg alloy nanoparticles with sizes between 3–13 nm, decorated on the surface of NG nanosheets. Electrochemical impedance spectroscopy (EIS) data also showed a decrease in the charge transfer resistance of Pd_1Ag_1/NG–GCE compared with Pd/NG, Ag/NG, NG and GCE, which suggests that the electron-transfer kinetics for MTX oxidation is highly facilitated at the Pd_1Ag_1/NG interface. The electrocatalytic activity of Pd_1Ag_1/NG–GCE towards MTX was also explored using cyclic voltammetry (CV) and differential pulse voltammetry (DPV) at pH 5.8. The anodic peak currents of MTX on Pd_1Ag_1/NG–GCE were approximately 8-fold higher than on the non-modified electrodes. A good linear ratio of the oxidation peak currents and MTX concentrations over the range of 0.02–200 μM with a limit of detection of 1.32 nM was achieved.

1. Introduction

The synthesis and characterization of nanostructured materials have attracted attention due to their high surface area and significantly different properties compared with coarse-sized conventional materials. Many studies have been carried out on the catalytic properties of noble metal nanoparticles [1] due to their large surface area, conductivity and chemical stability. However, most of the pure noble metals demonstrate poor selectivity, low sensitivity, which are important issues to be addressed for research applications. To further improve the sensitivity, selectivity and electrocatalytic performance of noble metal nanoparticles, secondary metals, such as Fe, Co, Ni, Sn and Ag, are combined with pure noble metals to form bimetallic alloys. Bimetallic alloys often exhibit superior catalytic performances compared to their monometallic counterparts due to the synergistic effect between the two metals and the high flexibility of chemical compositions and structures. The incorporation of multiple metals into a single system compared with the single metal element is useful for a wide range of applications; therefore, the fabrication of alloy nanoparticles has become a major research topic [2]. Based on this motivation, the choice of the noble metal or metal oxide for the synthesis of nanocomposites for catalytic and sensor applications is another essential factor which must be addressed. Palladium and silver are the common types of metals used as electrochemical sensors[3-6]. The relatively low cost and strong structural properties of silver make it an attractive material to combine with palladium for sensor applications, as well as for hydrogen purification and storage. Another method to improve the electrocatalytic activity of noble metal is to introduce a support material that facilitates electronic interactions between the support and the nobel metal nanoparticles. The materials that have been used as supports are carbon nanotubes [7, 8], carbon nanodots [9], carbon nanofibers [10], reduced graphene oxide [11-13] and conducting polymers [14-16]. Among the

support materials, graphene exhibits excellent properties as a matrix for the nanocomposites due to its large surface area, good electrical conductivity, good chemical stability and quick charge carrier mobility [17]. Previous reports have shown that chemical doping of graphene with foreign atoms, such as boron, nitrogen, fluorine, chlorine, phosphorus, and sulfur, manipulates the surface chemistry and introduces a considerable number of defects into the graphene lattice[18-21]. Due to the comparable atomic size and valence electrons of nitrogen [22], it can be used as an excellent dopant for graphene. Likewise, strong valence bonds can be formed between the nitrogen lone pair electrons and the graphene π-electron system. Therefore, nitrogen doping can enhance the formation of a band gap in the graphene energy levels. This method leads to a significant increase in the electron conductivity, spin density and charge distribution of the carbon atoms, which lead to the formation of an activation region on the graphene surface [23] that increases its ability to bind guest molecules. Doped nitrogen atoms can also provide efficient anchorsites for well dispersion of metallic nanoparticles on the surface of carbon support. The large surface area, defect density and abundant functional groups of N-graphene (NG) on the surface facilitate the adsorption of nanoparticles. Apart from excellent electrocatalytic activity, biocompatibility, high electronic conductivity, excellent chemical, mechanical and thermal stability demonstrated by NG, based on the previous work, NG, also has large surface area, which is necessary for the adsorption of more Ag nanodendrites by π-π stacking, PtRu nanoparticles and so on [22, 24]. This large surface area is attributed due to its two-dimensional carbon structure. This good advantage of NG encouraged us to use it as a platform for depositing bimetallic nanoparticles. Previous studies have shown that the presence of NG and noble metal nanoparticles have important applications in different types of electrochemical applications, such as sensors and catalysis[25-27]. Moreover, the synthesis of nanoscale composites composed of bimetallic alloys, graphene and conductive polymers as electrochemical sensors has been

reported [28]. In addition, there has been extraordinary progress in the discovery of sensitive analytical determination methods of pharmaceutically active compounds used in the diagnosis, prevention and treatment of human diseases. From this perspective, the use of noble metal nanoparticles in drug oxidation reactions has become an interesting topic due to their relatively good performance. Therefore, considerable efforts have been focused on developing simple and practical techniques to prepare PdAg electrocatalysts with enhanced performance for the analytical determination of certain drugs. Methotrexate (MTX) is an anti-folate analog, in a class of folic acid that can be widely used for the treatment of various neoplastic and acute lymphoblastic leukemia diseases[29, 30]. It has also been used as an effective anti-inflammatory and immune-suppressive drug for the cancer treatment of head and neck, breast and bladder respectively [31], rheumatoid arthritis, juvenile idiopathic arthritis and other diseases [32]. However, MTX is not often used clinically because of its toxicity which normally affects the renal, gastrointestinal lesions, liver, among others. Therefore, the design of highly sensitive equipment for the determination of MTX is of paramount important in clinical and pharmaceutical sectors. Several methodologies have been used for the analysis of MTX in pharmaceutical formulations and biological fluids[33-37], despite the fact that, these methods are time consuming, high cost and very low sensitivity which limit their application. In recent years electrochemical methods have given much considerations for the analysis of MTX due to their fast response, high sensitivity, accuracy, simplicity and low cost [29]. MTX exhibits slow direct electron transfer process at glassy carbon electrodes (GCEs), without any modification which leads to a lower detection sensitivity. Previous studies reported that, chemically modified electrodes enhance the electrochemical sensing performance and could be also used in the fabrication of ion sensors and biosensors [38]. Currently, nanomaterials such as carbon nanotubes (CNTs), nano-titania and Au nanoparticles have been used to develop

sensitive MTX electrochemical sensors [39]. Based on these findings nanomaterials can play a significant role in the construction of highly sensitive MTX sensors.

The current research demonstrates a facile and one–step method to synthesize composites of N-graphene decorated with a palladium silver bimetallic alloy (PdAg/NG–GCE) with different ratios of Pd and Ag in the presence of NG. To the best of our knowledge, there are no reports on the use of (PdAg/NG–GCE) nanocomposites for MTX monitoring.

2. Experimental methods

2.1. Chemicals

MTX, silver nitrate, potassium phosphate dibasic (K_2HPO_4) and potassium phosphate monobasic KH_2PO_4 were purchased from Sigma Aldrich. Palladium (II) nitrate dihydrate and all other chemicals (E. Merck, Germany) were of analytical grade and were used without further purification. Double-distilled water from a Millipore system was used in all experimental procedures.

2.2. Instrumentation and apparatus

All electrochemical measurements, such as electrochemical impedance spectroscopy (EIS), cyclic voltammetry (CV) and differential pulse voltammetry (DPV), were performed on a potentiostat/galvanostat (Autolab PGSTAT30, Ecochemie Netherlands). A GCE modified with nanocomposites of NG decorated with a palladium silver bimetallic alloy (PdAg/NG–GCE) was the working electrode, a platinum wire was the auxiliary electrode, and Ag/AgCl (3 M NaCl) was the reference electrode. Unless otherwise stated, all potentials are reported with respect to the reference. The CVs were scanned between 0.2 and 1.4 V at 20 mV s^{-1} in 0.1 M phosphate buffer solution (K_2HPO_4 and KH_2PO_4) at pH 5.8.

2.3. Synthesis of NG

NG was prepared using a procedure similar to a previous study [22]. GO, synthesized by the Hummers method [40], was used as the starting material. The GO dispersion (0.2 mg mL^{-1}) was sonicated in an ultrasonic bath for 30 min to obtain a yellow-brown dispersion. The chemical reduction method was initiated by adding 0.8 mL of hydrazine to 30 mL of GO dispersion. Then, the product was irradiated in a microwave oven on high power for 5 min to obtain a stable black dispersion of the NG sheets. The black NG sheets were collected by ultra-centrifugation of the NG suspension. Finally, the sample was dried in an oven at 50 ºC.

2.4. PdAg/NG– nanocomposite synthesis and electrode preparation

The nanocomposites were synthesized with different ratios of Pd and Ag (1:3, 1:1 and 1:2). In a typical process, 20 mL of 0.05 M $Pd(NO_3)_2.2H_2O$ and 20 mL of 0.05 M $AgNO_3$ aqueous solutions were added to 2 mL of NG suspension (10 mg mL^{-1}). The pH of the mixture was adjusted to 8 with the addition of sodium hydroxide (0.1 mol L^{-1}). The mixture was heated to 80 ºC with continuous stirring for 35 min before the addition of 0.01 mL of hydrazine monohydrate. This process was allowed to occur for another 30 min, during which the Pd and Ag were decorated on the surface of the NG nanosheets to form Pd_1Ag_1/NG. Finally, the suspension was cooled to room temperature and centrifuged at 4000 rpm for 15 min to separate the Pd_1Ag_1/NG from the solution, followed by drying in a vacuum oven at 60 °C for 24 h. The entire process was repeated for the synthesis of Pd/NG and Ag/NG.

The modified electrode was fabricated as follows: the prepared PdAg/NG (with different ratios of Ag and Pd), Pd/NG, Ag/NG and NG (1 mg) was dispersed separately in 1 mL of water with ultra-sonication for 1 h to obtain a homogenous suspension. Then, 15 µL of each homogenous suspension was dropped on the surface of a polished GCE separately and dried at room temperature.

2.5. Characterization methods

Phase composition of the composites with different Pd:Ag ratios was investigated by X-ray powder diffraction (XRD) using an automated diffractometer (PANalytical's Empyrean) with monochromated CuKa radiation (λ = 1.54056 °A). The particle size and structural characterization of PdAg/NG (with different ratios of Ag and Pd) were obtained by high-resolution transmission electron microscopy (HRTEM-FEIG-4020, 500 kV). The energy dispersive X-ray (EDAX) analysis was performed using an EDAX-System (Hitachi SU8000) instrument attached to a FESEM instrument to investigate the elemental composition of the samples.

2.6. Electrochemical measurements

The experiments were performed by studying the cyclic voltammetric behavior of the electrode in phosphate buffer (pH 5.8) as the supporting electrolyte between 0.2–1.4 V at 5–100 mV s^{-1}. EIS measurements were obtained in a frequency range of 0.1 Hz to 10^5 Hz with an AC voltage amplitude of 5 mV in a 0.1 M KCl solution containing 1 mM $[Fe(CN)_6]^{3-/4-}$ (1:1). The DPV was performed from 0.6 V to 1.4 V, with a step potential of 2 mV and a modulation amplitude of 50 mV at 10 mV s^{-1}. All experiments were conducted at 25 ± 5 ºC. It should be noted that all experiments were performed in compliance with the relevant laws and institutional guidelines, and the institutional committee(s) that has approved the experiments.

3. Results and discussions

3.1. TEM/HR-TEM and EDS analysis

One outstanding advantage of bimetallic alloys for use as a biosensor over the single metal counterpart lies in the chemical composition, which spans a wide range of measurement, and

causes a synergistic effect between the two components in catalytic applications. Nonetheless, the alterations in the atomic ratio of the components (two metals) may lead to dramatic changes in morphological features [41]. In the present work, the influence of different Pd/Ag atomic ratios in the presence of a fixed amount of NG on the morphological evolution is examined. For comparison, Pd/NG and Ag/NG hybrids were also prepared at the same reaction condition. Fig. 1 shows the TEM images of the hybrid structures and PdAg/NG nanocomposites with different Pd:Ag ratios. As shown in Fig. 1a, in the absence of $AgNO_3$, the reduction of $Pd(NO_3)_2.2H_2O$ with hydrazine produced non-uniform sized (from 5 to 10 nm) and spherical-shaped Pd, which is decorated on the surface of NG sheets. On the other hand, in the absence of $Pd(NO_3)_2.2H_2O$, well-dispersed rod-shaped Ag nanoparticles are deposited on NG sheets homogeneously, and the size range of Ag nanoparticles is mostly between 25–100 nm (Fig. 1b). From the HRTEM images (inset of Fig.1 a and b), the measured lattice fringe spacing of 0.24 nm in Pd and 0.23 nm in Ag nanoparticles correspond to the (111) crystal plane. After the deposition of Pd:Ag atomic ratio of 1:1, the individual PdAg alloy nanoparticles with sizes between 3–13 nm are well separated from each other and are well distributed on the NG nanosheets (Fig. 1c). This figure also shows that no large areas of the NG sheets remain undecorated with the PdAg alloy. As the Pd:Ag atomic ratio changed to 1:2 (Fig. 1e), the PdAg alloy nanoparticles revealed a high tendency to agglomerate due to the large surface to volume ratio of the nanoparticles, due to the Ostwald ripening effect [42]. When the two adjacent primary nanoparticles collide, coalescence may occur on the premise that these two nanoparticles share a common crystallographic orientation. Accordingly, two primary nanoparticles attach to each other and combine into a secondary nanoparticle. Because the sizes of the secondary nanoparticles are very small, it is reasonable that they will continue to collide and coalesce, which may ultimately lead to agglomeration [43]. Further increase of the Pd:Ag atomic ratio to 1:3 gave a more scattering

size distribution in the nanoparticles as shown in Fig. 1g. This shows that a lower content of Ag is favorable to improve the uniformity of morphology and size of PdAg alloy nanoparticles. From the HRTEM images in Fig. 1d, f and h, the distance (0.16 and 0.21 nm) between the adjacent lattice fringes are in accordance with the d_{200} and d_{111} spacing of the standard values. The above results indicate that Ag plays a key role in the formation of PdAg alloy nanoparticles, by finely tuning the molar ratio of Pd/Ag will result in well-defined and high-quality PdAg/NG nanocomposites. Considering the different standard reduction potential of Ag and Pd ions, the variation in the Pd/Ag atomic ratio has a significant effect on the nucleation process, which in turn affects the primary metal particle sizes and morphological changes of the nanocomposites. This result is in good agreement with the previous studies on Au−Cu[44] and Au−Pd[45] bimetallic alloys, where the presence of Cu and Pd also play an important role in inducing the nanowire and nanodendrite network morphologies. However, neither morphology nor size was uniform possibly because the nucleation rate was too fast to be controlled very well [45]. Therefore, it can be concluded that any attempts to accelerate bimetallic alloy nanoparticle formation by using hydrazine as a stronger reducing agent may lead to poor shape selectivity.

In this study, EDS analysis and elemental mapping were also utilized to investigate the elemental composition and distribution of the synthesized PdAg/NG nanocomposites. According to the EDS spectrum in Fig. 2a, the main elements of the nanocomposite are Pd, Ag, and C. Moreover, no chemically stable contaminants resulting from the reduction process are observed. The elemental mapping analysis indicates that Pd and Ag are homogeneously dispersed in the nanocomposite, indicating the formation of the alloy structure (Fig. 2b). Moreover, HRTEM and elemental mapping analysis strongly imply that the present PdAg/NG nanocomposites are composed of multiple crystalline domains.

<Fig. 1>

<Fig. 2>

3.2. Phase composition and structural evaluation

The crystalline structure of the PdAg/NG nanocomposite was further examined with XRD analysis. Fig. 3a displays the XRD patterns of the products with different Pd:Ag molar ratios. For comparison, the standards (Pd: 046-1043 and Ag: 004-0783) compiled by the Joint Committee on Powder Diffraction and Standards (JCPDS) are also included. From the XRD profiles, it is obvious that all the characteristic peaks of the raw materials have completely disappeared, and only the diffraction peaks corresponding to the (1 1 1), (2 0 0), (2 2 0) and (3 1 1) planes are detected. It can be clearly seen that compared with the standard data, the diffraction peaks of the PdAg/NG nanocomposite shift to lower 2Θ values, signifying a reduction in the lattice constant. It should be noted that all the diffraction peaks of the PdAg/NG nanocomposites are located between the positions expected for the pure Pd and Ag, which confirms the alloying of Pd and Ag. This result is in good agreement with previous studies [46-48]. In addition, neither a Pd nor Ag single component peak is observed, suggesting that the PdAg alloys are of high purity. It should also be mentioned that from the standard XRD pattern of Pd, the intensity ratio between the diffraction peaks of (1 1 1) and (2 0 0) is 1.66, but for the nanocomposite with Pd:Ag molar ratios of 1:1, 1:2 and 1:3, the ratio increases to 3.76, 4.58 and 3.13, respectively. This shows the abundant (1 1 1) planes of the PdAg in the nanocomposite structure, which is consistent with the (1 1 1) interplanar spacing found in the HRTEM measurements (Fig. 1). Fig. 3b illustrates the variation in XRD profiles between $2\theta = 35°–42°$ for the nanocomposite with different Pd:Ag molar ratios. It is obvious that the intensity of the characteristic peaks of the PdAg alloy enhances significantly with the change of the Pd:Ag molar ratio from 1:1 to 1:3, which is due to the crystallization of the composite during the synthesis process. The structural features of the products are shown in Figs. 3c and 3d. It is clear that the crystallite size and micro-strain of the as-synthesized

nanocomposites are significantly affected by the molar ratio of Pd:Ag. With a Pd:Ag molar ratio of 1:1, the crystallite size and lattice strain is 31±2 nm and 0.257%, respectively. When the molar ratio of Pd:Ag changes to 1:2 and 1:3, the crystallite size reaches 28±2 and 48±2 nm, respectively.

<Fig. 3>

3.3. Raman spectroscopy

Raman spectroscopy is a powerful technique for the investigation of the structural and electronic properties of carbon compounds. Accordingly, GO, NG and Pd_1Ag_1/NG structures were further studied by Raman spectroscopy to detect the doping effects of graphene materials (Fig. S1). The spectra of GO and NG show three features: the D, G and 2D bands are centered at approximately 1346 cm^{-1}, 1597 cm^{-1} and 2698 cm^{-1} for GO, whereas they are centered at 1335 cm^{-1}, 1577 cm^{-1} and 2686 cm^{-1} for NG, respectively. In addition to these three peaks, NG presents a weak D' band located at 1695 cm^{-1}. This shows that the nitrogen doping in the graphene lattice leads to the presence of a D' band in the Raman spectrum of NG. In these spectra, the G and 2D bands arise from the in-plane bond stretching of the C-C sp^2 bond, whereas the D and D' bands (activated by inter-valley and intra-valley double-resonant Raman processes, respectively) are associated with various types of defects, such as vacancy-like defects and sp^3 defects, that can be produced by oxidation and hydrogenation, grain boundary edges, domain boundaries and electron doping. In the case of GO and NG, the presence of a sharp D peak shows the generation of high defect levels (edges, defects, functionalities), while the characteristic strong G band and the weak 2D-peak reveal the vibration of the sp^2-bonded carbon atoms in the two-dimensional hexagonal lattice. On the other hand, the Raman spectrum of the Pd_1Ag_1/NG composite indicates some changes compared to GO and NG. The changes in G band spectral position and the broadening of the

characteristic bands are more interesting because the G and D bands are sensitive to defects, disorder and carbon grain size. Generally, I_D/I_G is a measure of the disordered carbon and the average size of the sp^2 domains, as expressed by the sp^3/sp^2 carbon ratio and an increase of the I_D/I_G is due to the degradation of crystallinity of graphitic materials [49]. The intensity ratio of the D to G bands (I_D/I_G) increased from 0.65 for GO to 0.87 for NG, where nitrogen doping led to the increase of defects in graphene after the microwave-assisted reaction. However, the intensity of the 2D band in pristine GO is higher than that in NG; thus, the intensity ratio of the 2D to G band (I_{2D}/I_G) decreases for GO compared with NG, which confirms the increase in the defect density and the successful reduction of GO. Note that the intensity of the 2D band is reciprocal to the electron-hole scattering rate. Thus, nitrogen doping creates defects in the graphene lattice, which leads to an increase in the electron-hole scattering and a decrease in the 2D band intensity. For the Pd_1Ag_1/NG composite, the I_D/I_G (1.17) of NG is clearly higher than that of the pure GO and NG, indicating that there are more defects or disorders in the NG. This feature is likely to be influenced by the synthesis process.

3.4. EIS studies

Electrochemical impedance spectroscopy (EIS) is a useful method to investigate the characteristics of the modified electrode-electrolyte interface. The application of a low amplitude alternating voltage (*V*) leads to a sinusoidal output current (*I*). The electrochemical impedance (*Z*) is defined as follows:

$$Z = \frac{V}{I} = \frac{V(t)}{I(t)} = \frac{V_m \sin(\omega t)}{I_m \sin(\omega t + \varphi)} = Z_0 \frac{\sin(\omega t)}{\sin(\omega t + \varphi)} = Z' + jZ'' \quad (5)$$

where Z'' and Z' are defined as the imaginary and the real part of the impedance, respectively. The electrical conductivity of the bare, NG, Pd/NG, Ag/NG and Pd_1Ag_1/NG modified GCEs was studied by electrochemical impedance spectroscopy (EIS) in an $[Fe(CN)_6]^{3-/4-}$ solution. Fig. 4 shows the Nyquist plots of the modified electrodes. The electron transfer resistance

(R_{ct}) can be directly measured from the semicircle diameter. The R_{ct} value increases with the surface modification of GCE with GO compared with the bare GCE, which suggests that GO plays a role as an insulating layer against the electron transfer process due to the disruption of the sp^2 bonding networks [50, 51]. The abundance of the negatively charged oxygen-containing groups in GO restricts the $[Fe(CN)_6]^{3-/4-}$ from reaching the electrode. With the alteration of graphene by doped N through chemical reduction with hydrazine, the charge transfer resistance decreases, which can be explained by the preservation of small band gaps favorable for the electron transfer process. With the incorporation of Ag or Pd nanoparticles in NG, the R_{ct} value decreases dramatically, which indicates that NG decorated with Pd and Ag nanoparticles accelerates the electron transfer process between the modified electrode and $[Fe(CN)_6]^{3-/4-}$. The primary reason for this can be attributed to a significantly improved electrical conductivity of the NG sheets in the presence of Pd or Ag nanoparticles. The R_{ct} value of the Pd_1Ag_1/NG-modified GCE effectively decreases, which illustrates the successful incorporation of Ag and Pd nanoparticles on the surface of the NG nanosheets. The anchoring of Ag and Pd nanoparticles on the surface of the NG sheets introduced positively charged Ag^+ and Pd^+, which efficiently separates the NG sheets and attracts negatively charged $[Fe(CN)_6]^{3-/4-}$. The higher conductivity of the Ag and Pd nanoparticles and the synergistic effect of Ag, Pd and NG are the main reasons for the increase in the conductivity of the modified electrodes. A comparison between the semicircle diameters from the Nyquist plots of the bare GCE, GO, NG, Pd/NG, Ag/NG and Pd_1Ag_1/NG shows the decrease of the R_{ct} in the following order:

GO > GCE > NG > Pd/NG> Ag/NG> Pd_1Ag_1/NG

Figure S2 (A) shows the Bode diagram of the samples and confirms the proposed R_{ct} order. Fig S2 (B) show the equivalent circuits.

<**Fig. 4**>

3.5. Electrochemical behavior of MTX

Fig. 5 shows the comparison between the catalytic activities of modified PdAg/NG–GCE electrodes prepared under similar conditions with different ratios of Pd and Ag. Recently, it was reported that the presence of Ag in bimetallic nanocrystals with Pd enhances the surface activation for the electrooxidation of MTX. The observations show that the modified GCE of PdAg/NG (1:1) (Fig. 5c) has high catalytic activity toward MTX electrooxidation compared with the modified PdAg/NG–GCE with composite ratios of 1:2 (Fig. 5b) and 1:3 (Fig. 5a). The higher electrocatalytic activity of Pd_1Ag_1/NG can be related to the increase of the ratio of Ag in the bimetallic nanocrystals, as the catalytic performance decreases due to lower activity of Ag to MTX electrooxidation. As shown, the current is more prominent for Pd_1Ag_1/NG–GCE, indicating that the effective surface area of PdAg/NG–GCE is larger with a 1:1 ratio than with the other two ratios.

The performance of Pd_1Ag_1/NG–GCE was investigated by cyclic voltammetry in a 0.1 M phosphate buffer solution (pH 5.8) in the presence of 100 μM MTX. It can be clearly observed that the bare GCE has the weakest response for the detection of MTX. The broad redox coupled peaks of MTX on the bare GCE, NG–GCE, Ag/NG–GCE and Pd/NG–GCE (Fig. 6a–d) indicate a slow electron transfer process. The Ag/NG–GCE and Pd/NG–GCE (Figs. 6c and 6d) have larger peak currents compared with the bare GCE (Fig. 6a) and NG–GCE (Fig. 6b). The reason for the enhanced oxidation of MTX at the Ag/NG–GCE and Pd/NG–GCE compared with the NG–GCE could be due to the increase in the surface area of NG due to the presence of Ag NPs and Pd NPs because the deposition of Ag NPs and Pd NPs on NG sheets effectively increases the total surface area of NG. It is obvious that the increase in the peak currents of Pd_1Ag_1/NG–GCE (Fig. 6e) compared with the other electrodes is due to the large increase in the area of the electrode surface modified with Pd, Ag and NG. These

results confirm that nitrogen doping in the graphene lattice in the presence of Ag NPs and Pd NPs can improve the electrocatalytic activity of graphene toward MTX oxidation.

Fig. S3A indicates the effect of pH of the phosphate buffer solution on the oxidation current of MTX on Pd_1Ag_1/NG–GCE. The current dramatically increases as the pH increases from 3 to 5.8 and gradually decreases for a pH value higher than 5.8. Therefore, pH 5.8 was selected as the optimum pH for the electrochemical oxidation of MTX.

The effect of the phosphate buffer pH on E_{pa} (anodic peak potential) was investigated, and the results show that E_{pa} was shifted toward negative potentials with a slope of -59 mV per decade. A linear relationship of E_{pa} (V) = -0.059 pH +1.38 was obtained with R^2 = 0.992 (Fig. S3B). The slope is notably close to the Nernstian value of -59 mV per decade, which suggests that the numbers of protons and electrons transferred in the redox reaction of MTX are equal. Two electrons and two protons are involved in the oxidation of MTX. Thus, the mechanism of the redox process of MTX is proposed in Scheme 1 [52].

The scan rate dependency of the modified electrode in 100 μM MTX was also investigated. Fig. 7 shows the CVs in a 0.1 M phosphate buffer solution (pH 5.8) containing 100 μM MTX on Pd_1Ag_1/NG–GCE at different scan rates from 5 to 100 mV s^{-1}. As the scan rate increases, the MTX oxidation peak slightly shifts toward the positive region, with an increase in the peak current. A linear relationship between the oxidation current and the square root of the scan rate is expressed using the following linear regression equation: I_{pa}/ μA =414.4X - 298.52v/mV s^{-1} (R^2 = 0.998). These results indicate that the oxidation of MTX on Pd_1Ag_1/NG–GCE is a diffusion-controlled process [53].

<Fig. 5>

<Fig. 6>

<Fig. 7>

<Scheme 1>

3.6. Determination of MTX using differential pulse voltammetry

Fig. 8 shows the differential pulse voltammogram of different concentrations of MTX in 0.1 M phosphate buffer (pH 5.8) between 0.6–1.4 V with a step potential of 2.0 mV and a modulation amplitude of 50 mV at 10 mV s^{-1}. The anodic peak current, I_{pa}, is linearly proportional to the MTX concentration over the range of 0.02–200 μM. A linear equation of I_{pa} (μA) =13.568[MTX] (μM) + 288.476 with (R^2= 0.999) was obtained. The detection limit of MTX at the Pd_1Ag_1/NG–GCE is 1.32 nM.

<Fig. 8>

3.7. Interference effects

The effect of common interfering species in biological samples on Pd_1Ag_1/NG–GCE modified electrode was studied. Fig. 9. shows the amperometric response of the modified electrode toward addition of 100 μM MTX and this is followed by 100 μM of uric acid (UA), ascorbic acid (AA), glucose and dopamine[54, 55] into 0.1 M phosphate buffer solution (pH 5.8). As can be seen in the figure, the interfering substances responded with very weak signals which demonstrate that the modified electrode has a good selectivity toward MTX. Nonetheless, when 100 μM MTX is spiked into the phosphate buffer solution with UA, AA, glucose and dopamine, I_{pa} sharply increases. The results indicate that the Pd_1Ag_1/NG has high selectivity towards MTX detection, even in the presence of some common interfering compounds that are normally found in biological samples.

Table 1 shows a comparison between the results of this study and other studies for MTX determination. This table also shows the result of sensing performance of Ag/NG–GCE, Pd/NG–GCE compared with Pd_1Ag_1/NG–GCE for MTX. The linear range of prepared sensor (0.02 –200 μM) is considerably greater than that of other studies[29, 56, 57]. The limit of detection of MTX at the Pd_1Ag_1/NG–GCE shows better sensitivity than that in previous

reports and also Ag/NG–GCE and Pd/NG–GCE. The high sensitivity, wide linear range and low detection limit can be attributed to the presence of Ag in the anchoring bimetallic nanocrystals with Pd on NG sheets and moreover existing NG as a substrate enhances the conductivity of the system and effective surface area. Graphene composites with bimetallic alloy revealed high catalytic activity in the fabrication of nanoscale sensors.

<Fig. 9>

<Table 1>

3.8. Analysis of real samples

3.8.1. The analytical determination of MTX in urine samples

To determine the accuracy of the sensor, the sensor was utilized for the determination of MTX in three human urine samples using the standard addition method. Because MTX was not found in healthy human urine samples, a recovery experiment was performed by adding certain amounts of an MTX standard solution to the diluted urine samples of healthy specimens. The non-pretreated samples (250 mL) with mid-range values are diluted 30 times with phosphate buffer (pH 5.8). The calculated recovery and relative standard deviation (RSD) values from Table S1 show that the prepared sensor can be used to determine certain concentration ranges of MTX.

3.9. Reproducibility, repeatability and stability

The repeatability, reproducibility and stability of the prepared sensor were also studied. Seven modified electrodes were prepared under the same conditions, with a relative standard deviation (RSD) of the current response toward 100 μM MTX of 2.21%, confirming that the results are reproducible. The repeatability of the sensor for the determination of 100 μM MTX was relatively good, and the RSD was 1.68% for 10 successive assays. To investigate

the stability of Pd_1Ag_1/NG–GCE, the modified electrode was stored under ambient conditions, and the current was periodically monitored for 21 days (Fig. S4). The current did not show a considerable decrease in the first week, and from Fig. S4, the sensor retains approximately 86.3% of its initial response after 3 weeks (I_0 and I are the current response for the first and following days, respectively). The overall performance concluded that Pd_1Ag_1/NG–GCE shows good reproducibility, repeatability and stability.

4. Conclusions

Composites of NG decorated with a palladium silver bimetallic alloy (PdAg/NG–GCE) with different ratios of Pd and Ag (1:3, 1:1 and 1:2) were synthesized. The results demonstrated that PdAg/NG–GCE with a Pd:Ag ratio of 1:1 gave superior electrocatalytic activity toward MTX electrooxidation compared with Pd/NG, Ag/NG, NG and GCE. This is due to the presence of Ag in the anchoring bimetallic nanocrystals with Pd on NG sheets, which enhances the effective surface area. The impedance data confirmed that the charge transfer resistance (R_{ct}) of the modified electrode was significantly decreased. Additionally, Pd_1Ag_1/NG–GCE exhibits a lower detection limit for MTX oxidation, with improvement in the anodic peak current. The proposed method was successfully applied to the determination of MTX in human urine with good precision and accuracy. These improved performances, such as high selectivity and sensitivity, ease of fabrication and, especially, wide linear range, make Pd_1Ag_1/NG–GCE an excellent sensor for the determination of the MTX concentration at nM levels.

Acknowledgments

The authors wish to thank the University of Malaya for providing funds for this research through GC001C-14SBS, RP038C-15HTM and RP007C-13AFR. The authors are also grateful to Research Affairs of Islamic Azad University, Najafabad Branch for supporting of this research.

References:

1. M. Akhtari Zavareh, A. A. D. M. Sarhan, B. B. Razak and W. J. Basirun, *Ceram. Int.*, 2015, **41**, 5387-5396.

2. T. Wu, J. Ma, X. Wang, Y. Liu, H. Xu, J. Gao, W. Wang, Y. Liu and J. Yan, *Nanotechnology*, 2013, **24**, 125301.

3. V. R. R. Medicherla and W. Drube, *Appl. Surf. Sci.*, 2009, **256**, 376-379.

4. W.-H. Lin and H.-F. Chang, *Surf. Coat. Technol.*, 2005, **194**, 157-166.

5. A. K. M. Fazle Kibria and Y. Sakamoto, *Int. J. Hydrogen Energy*, 2000, **25**, 853-859.

6. L. S. McLeod, F. L. Degertekin and A. G. Fedorov, *J. Membr. Sci.*, 2009, **341**, 225-232.

7. W. Yang, X. Wang, F. Yang, C. Yang and X. Yang, *Adv. Mater.*, 2008, **20**, 2579-2587.

8. F. Lorestani, Z. Shahnavaz, P. Mn, Y. Alias and N. S. A. Manan, *Sens. Actuat. B*, 2015, **208**, 389-398.

9. W. Wei and W. Chen, *J. Power Sources*, 2012, **204**, 85-88.

10. G. Hu, F. Nitze, H. R. Barzegar, T. Sharifi, A. Mikołajczuk, C.-W. Tai, A. Borodzinski and T. Wågberg, *J. Power Sources*, 2012, **209**, 236-242.

11. P. Moozarm Nia, W. P. Meng, F. Lorestani, M. R. Mahmoudian and Y. Alias, *Sens. Actuat. B*, 2015, **209**, 100-108.

12. P. Moozarm Nia, F. Lorestani, W. P. Meng and Y. Alias, *Appl. Surf. Sci.*, 2015, **332**, 648-656.

13. W. J. Basirun, M. Sookhakian, S. Baradaran, Z. Endut, M. R. Mahmoudian, M. Ebadi, R. Yousefi, H. Ghadimi and S. Ahmed, *Scientific reports*, 2015, **5**, 1-7.

14. R. M. Crooks, M. Zhao, L. Sun, V. Chechik and L. K. Yeung, *Acc. Chem. Res.*, 2001, **34**, 181-190.

15. M. Rezayi, Y. Lee, A. Kassim, S. Ahmadzadeh, Y. Abdollahi and H. Jahangirian, *Chem Cent J*, 2012, **6**, 40.

16. M. Rezayi, R. Karazhian, Y. Abdollahi, L. Narimani, S. B. T. Sany, S. Ahmadzadeh and Y. Alias, *Scientific reports*, 2014, **4**.

17. A. A. Abraham, M. Rezayi, N. S. A. Manan, L. Narimani, A. N. B. Rosli and Y. Alias, *Electrochim. Acta*, 2015, **165**, 221-231.

18. D. Deng, X. Pan, L. Yu, Y. Cui, Y. Jiang, J. Qi, W.-X. Li, Q. Fu, X. Ma and Q. Xue, *Chem. Mater.*, 2011, **23**, 1188-1193.

19. D. Wei, Y. Liu, Y. Wang, H. Zhang, L. Huang and G. Yu, *Nano Lett.*, 2009, **9**, 1752-1758.

20. N. Li, Z. Wang, K. Zhao, Z. Shi, Z. Gu and S. Xu, *Carbon*, 2010, **48**, 255-259.

21. M. Sookhakian, Y. M. Amin, R. Zakaria, S. Baradaran, M. R. Mahmoudian, M. Rezayi, M. T. Tajabadi and W. J. Basirun, *Ind. Eng. Chem. Res.*, 2014, **53**, 14301-14309.

22. M. T. Tajabadi, W. J. Basirun, F. Lorestani, R. Zakaria, S. Baradaran, Y. M. Amin, M. R. Mahmoudian, M. Rezayi and M. Sookhakian, *Electrochim. Acta*, 2015, **151**, 126-133.

23. P. Wu, Y. Qian, P. Du, H. Zhang and C. Cai, *J. Mater. Chem.*, 2012, **22**, 6402-6412.

24. X. Xu, Y. Zhou, J. Lu, X. Tian, H. Zhu and J. Liu, *Electrochim. Acta*, 2014, **120**, 439-451.

25. H.-J. Kim, S. H. Park and H.-J. Park, *Sensor Lett*, 2011, **9**, 59-63.

26. L. Kabir and S. Mandal, *Eur. Phys. J. Appl Phys* 2012, **58**, 20402.

27. E. Park, O. s. Kwon, S. j. Park, J. s. Lee, S. You and J. Jang, *J. Mater. Chem.*, 2012, **22**, 1521-1526.

28. H. Ghadimi, M. R. Mahmoudian and W. J. Basirun, *RSC Advances*, 2015, **5**, 39366-39374.

29. S. Wang, Z. Qi, H. Huang and H. Ding, *Anal. Lett.*, 2012, **45**, 1658-1669.

30. J. C. Panetta, A. Wall, C.-H. Pui, M. V. Relling and W. E. Evans, *Clin cancer res* 2002, **8**, 2423-2429.

31. R. Takata, T. Katagiri, M. Kanehira, T. Tsunoda, T. Shuin, T. Miki, M. Namiki, K. Kohri, Y. Matsushita and T. Fujioka, *Clin cancer res* 2005, **11**, 2625-2636.

32. E. Tanaka, A. Taniguchi, W. Urano, H. Yamanaka and N. Kamatani, *Best Pract Res Cl Rh*, 2004, **18**, 233-247.

33. B. Rafique, A. M. Khalid, K. Akhtar and A. Jabbar, *Biosens. Bioelectron.*, 2013, **44**, 21-26.

34. S. Chen, Z. Zhang, D. He, Y. Hu, H. Zheng and C. He, *Luminescence*, 2007, **22**, 338-342.

35. D. A. El-Hady, N. A. El-Maali, R. Gotti, C. Bertucci, F. Mancini and V. Andrisano, *J. Pharm. Biomed. Anal.*, 2005, **37**, 919-925.

36. I. D. Merás, A. E. Mansilla and M. J. R. Gómez, *Anal. Biochem.*, 2005, **346**, 201-209.

37. J. R. Flores, G. C. Peñalvo, A. E. Mansilla and M. R. Gómez, *J. Chromatogr. B*, 2005, **819**, 141-147.

38. Q. Wan, X. Wang, F. Yu, X. Wang and N. Yang, *J. Appl. Electrochem.*, 2009, **39**, 785-790.

39. H. Jiang and X.-M. Wang, *Electrochem. Commun.*, 2009, **11**, 126-129.

40. M. Sookhakian, Y. M. Amin, S. Baradaran, M. T. Tajabadi, A. M. Golsheikh and W. J. Basirun, *Thin Solid Films*, 2014, **552**, 204-211.

41. J. Han, Z. Zhou, Y. Yin, X. Luo, J. Li, H. Zhang and B. Yang, *CrystEngComm*, 2012, **14**, 7036-7042.

42. M. Sookhakian, Y. Amin, W. Basirun, M. Tajabadi and N. Kamarulzaman, *J Lumin*, 2014, **145**, 244-252.

43. P. Balaz, *Mechanochemistry in nanoscience and minerals engineering*, Springer Science & Business Media, 2008.

44. L. Shi, A. Wang, Y. Huang, X. Chen, J. J. Delgado and T. Zhang, *Eur. J. Inorg. Chem*, 2012, **2012**, 2700-2706.

45. L. Shi, A. Wang, T. Zhang, B. Zhang, D. Su, H. Li and Y. Song, *J. Phys. Chem. C,* , 2013, **117**, 12526-12536.

46. B. N. Wanjala, J. Luo, R. Loukrakpam, B. Fang, D. Mott, P. N. Njoki, M. Engelhard, H. R. Naslund, J. K. Wu and L. Wang, *Chem. Mater.*, 2010, **22**, 4282-4294.

47. Y. Lu and W. Chen, *Chem. Commun.*, 2011, **47**, 2541-2543.

48. Y. Lu and W. Chen, *ACS Catal*, 2012, **2**, 84-90.

49. S. Pei and H.-M. Cheng, *Carbon*, 2012, **50**, 3210-3228.

50. Y. Hu, F. Li, X. Bai, D. Li, S. Hua, K. Wang and L. Niu, *Chem. Commun.*, 2011, **47**, 1743-1745.

51. Y. Hua, S. Huab, F. Lia, Y. Jianga, X. Baib, D. Lib and L. Niua, *Biosens. Bioelectron.*, 2011, **26**, 4355-4361.

52. A. Pontinha, S. Jorge, V. Diculescu, M. Vivan and A. Oliveira-Brett, *Electroanalysis*, 2012, **24**, 917-923.

53. C. Wang, J. Du, H. Wang, C. e. Zou, F. Jiang, P. Yang and Y. Du, *Sens. Actuat. B*, 2014, **204**, 302-309.

54. Z. Zhu, F. Wang, F. Wang and L. Xi, *J. Electroanal. Chem*, 2013, **708**, 13-19.

55. Y. Wang, H. Liu, F. Wang and Y. Gao, *J. Solid State Electrochem.*, 2012, **16**, 3227-3235.

56. Y. Wang, J. Xie, L. Tao, H. Tian, S. Wang and H. Ding, *Sens. Actuat. B*, 2014, **204**, 360-367.

57. Y. Guo, Y. Chen, Q. Zhao, S. Shuang and C. Dong, *Electroanalysis*, 2011, **23**, 2400-2407.

Figure and Figure captions:

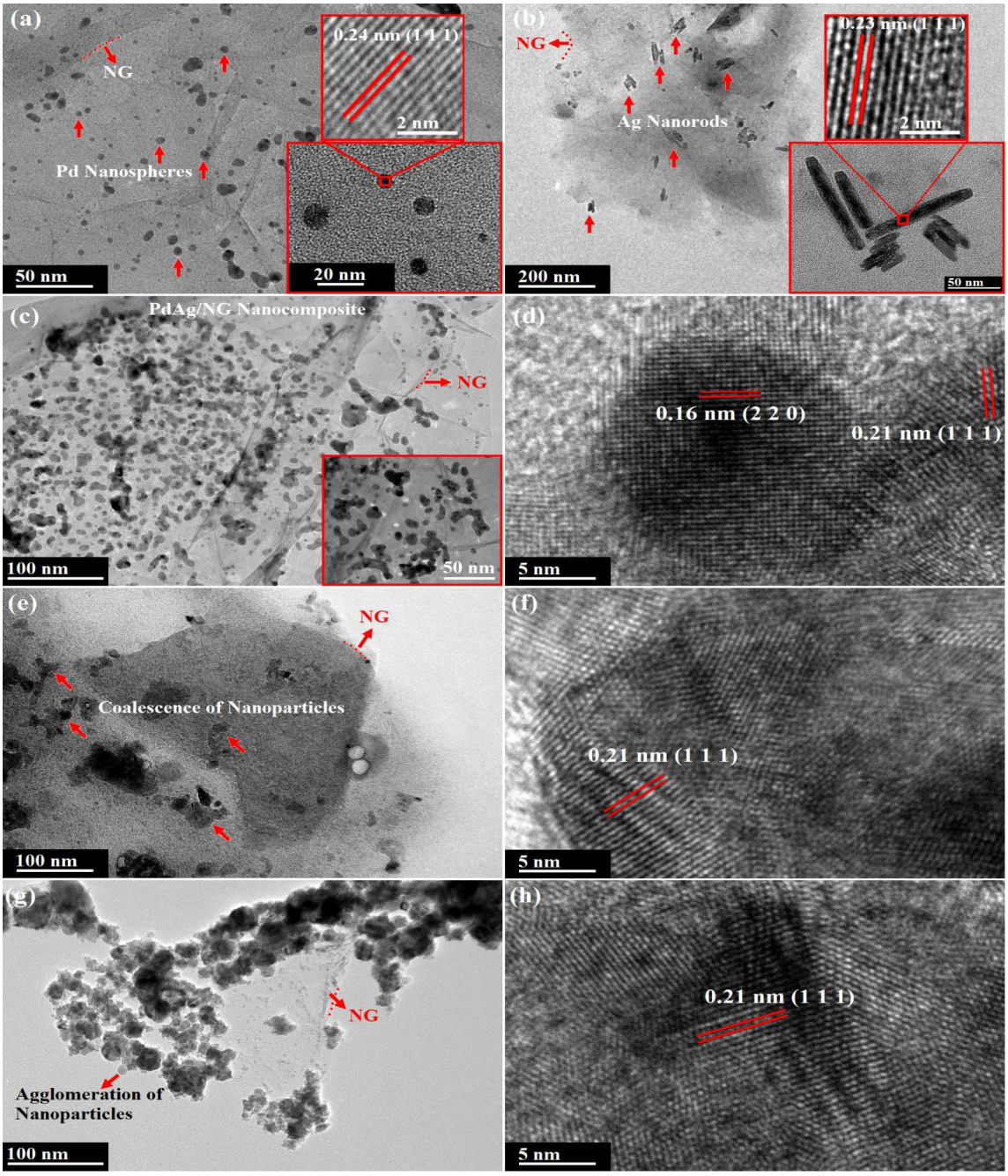

Fig. 1. TEM micrographs of the as-prepared (a) Pd/NG and (b) Ag/NG hybrids, as well as TEM/HRTEM images of PdAg/NG nanocomposites with different Pd:Ag ratios: (c,d) 1:1, (e,f) 1:2 and (g,h) 1:3

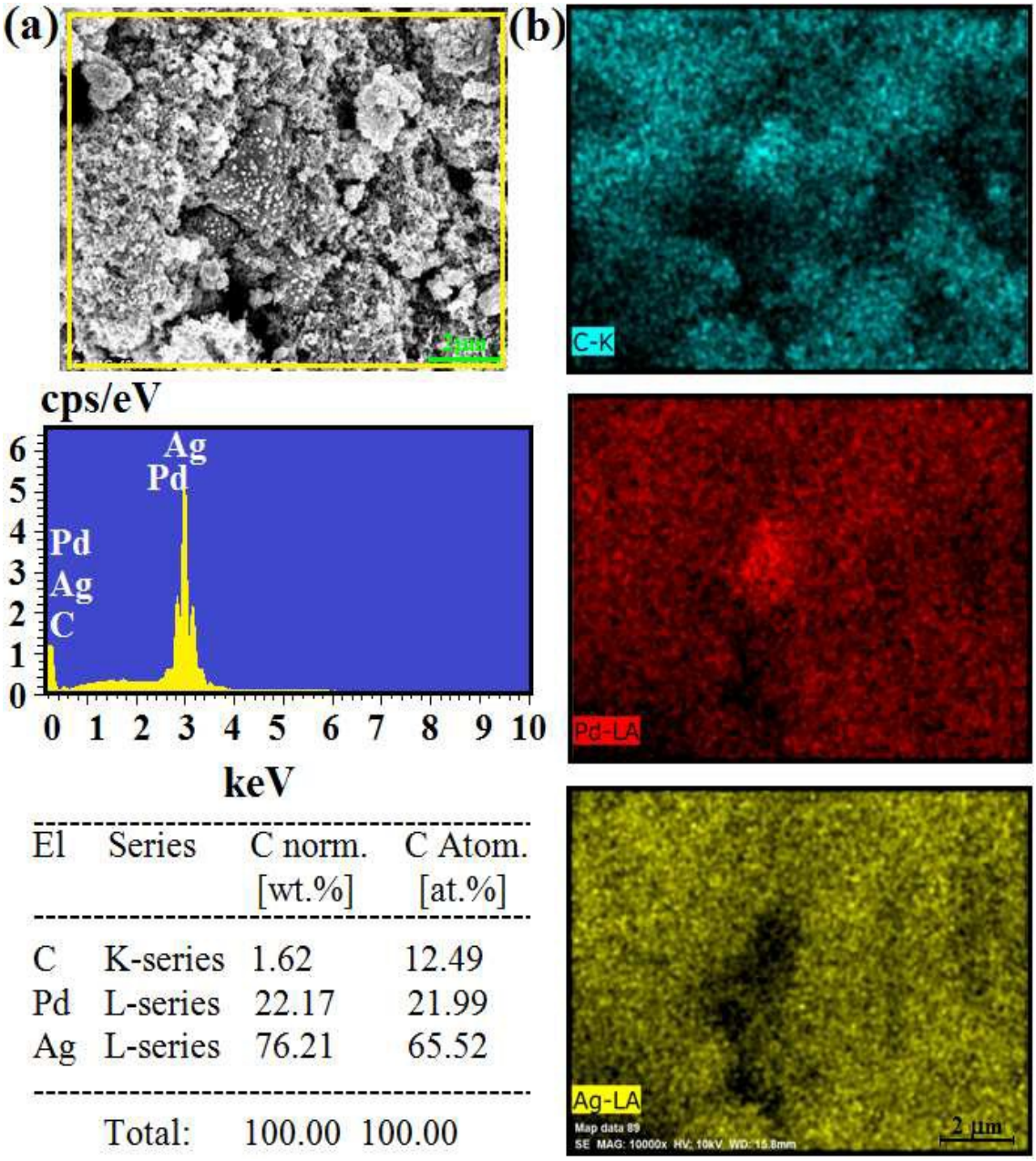

El	Series	C norm. [wt.%]	C Atom. [at.%]
C	K-series	1.62	12.49
Pd	L-series	22.17	21.99
Ag	L-series	76.21	65.52
	Total:	100.00	100.00

Fig. 2. (a) EDS analysis and (b) elemental mapping of the synthesized Pd_1Ag_1/NG nanocomposite.

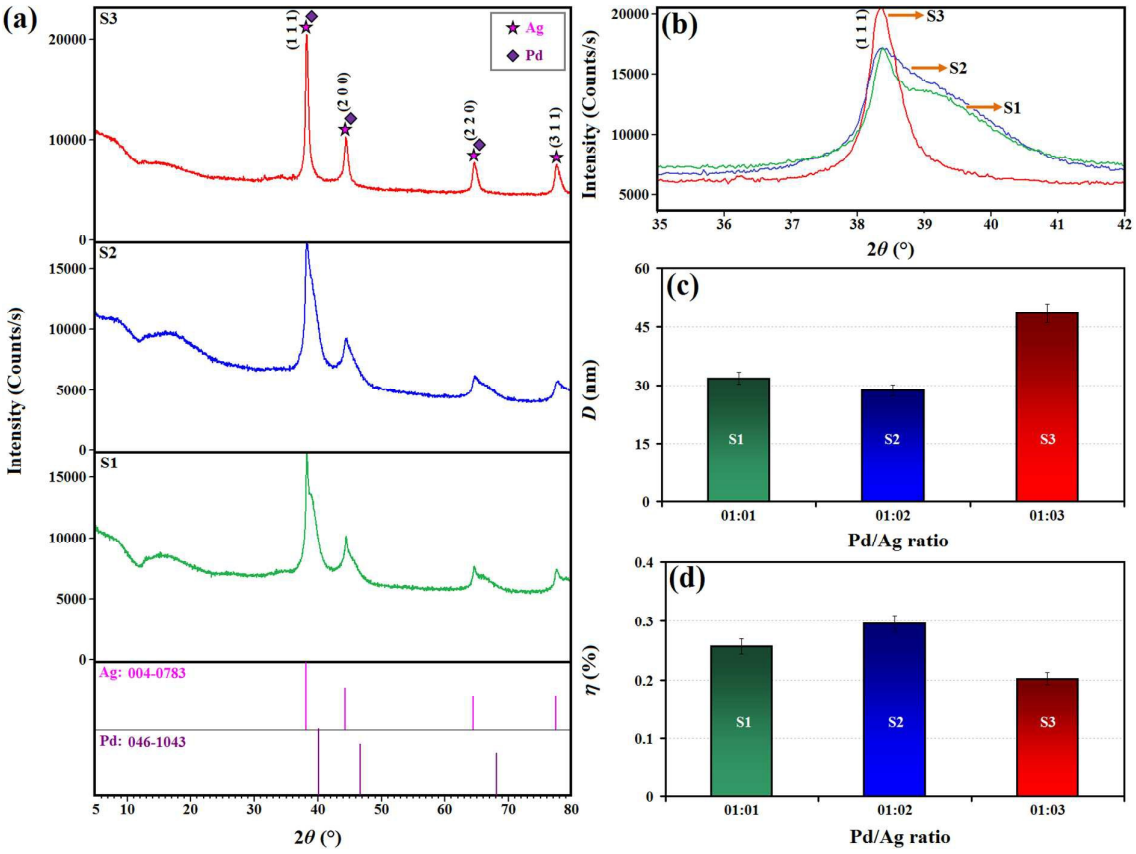

Fig. 3. (a) XRD patterns of the nanocomposites with different Pd:Ag molar ratios, (b) magnified XRD profiles in the range of $2\Theta = 35°–42°$, and structural features of the products (c) crystallite size (nm) and (d) lattice strain (%).

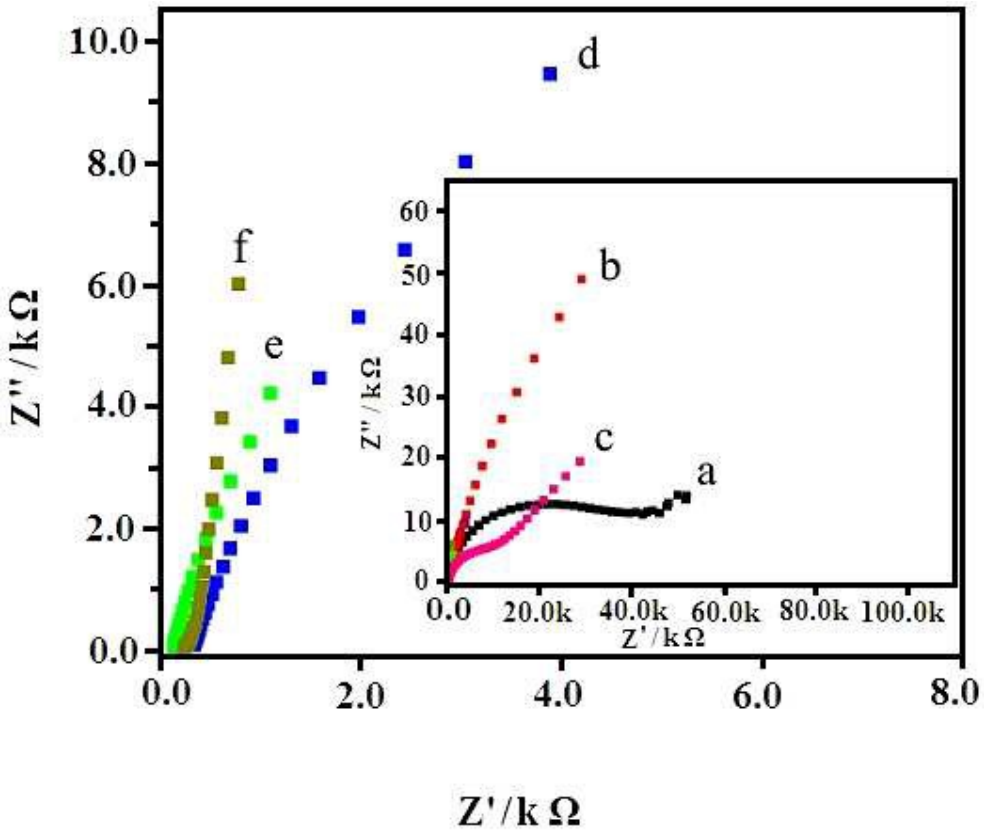

Fig. 4. (A) Nyquist plots of (a) bare, (b) GO, (c) NG, (d) Pd/NG, (e) Ag/NG and (f) Pd_1Ag_1/NG.

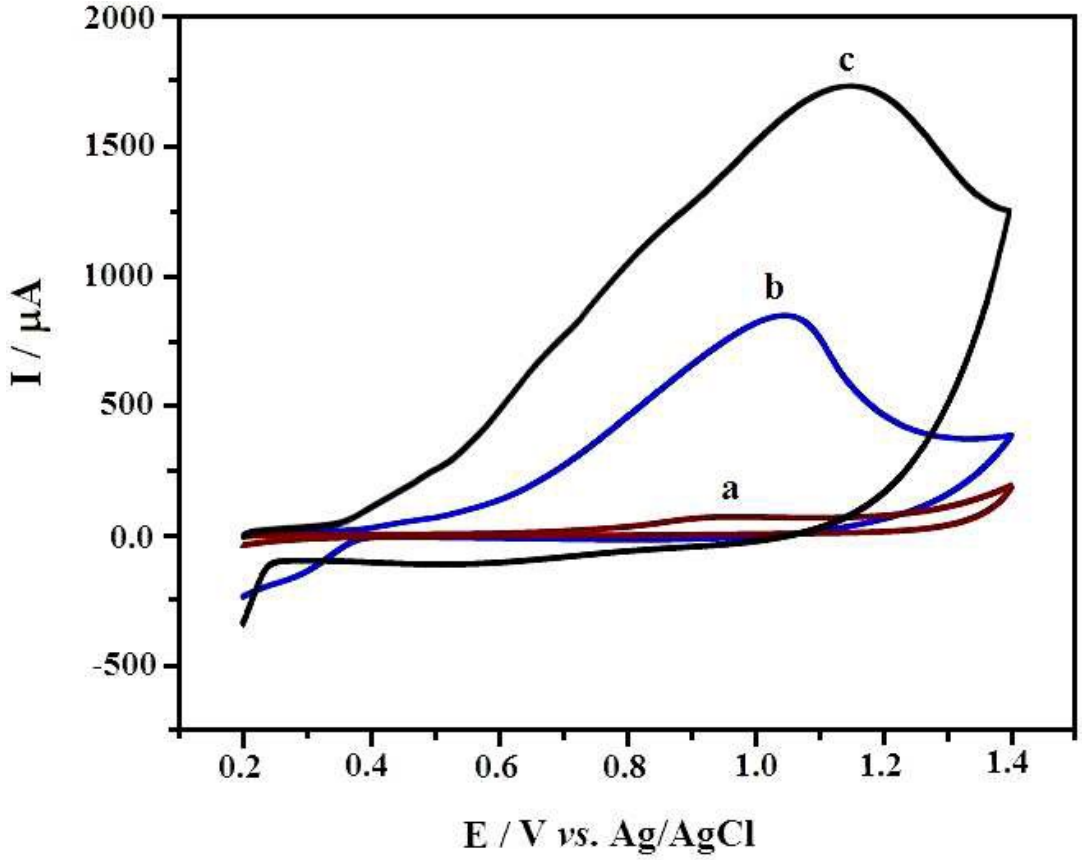

Fig. 5. CVs of PdAg/NG–GCE in a 0.1 M phosphate buffer solution (pH 5.8) in the presence of 100 μM MTX with different ratios of Pd:Ag: a: (1:3), b: (1:2), c: (1:1).

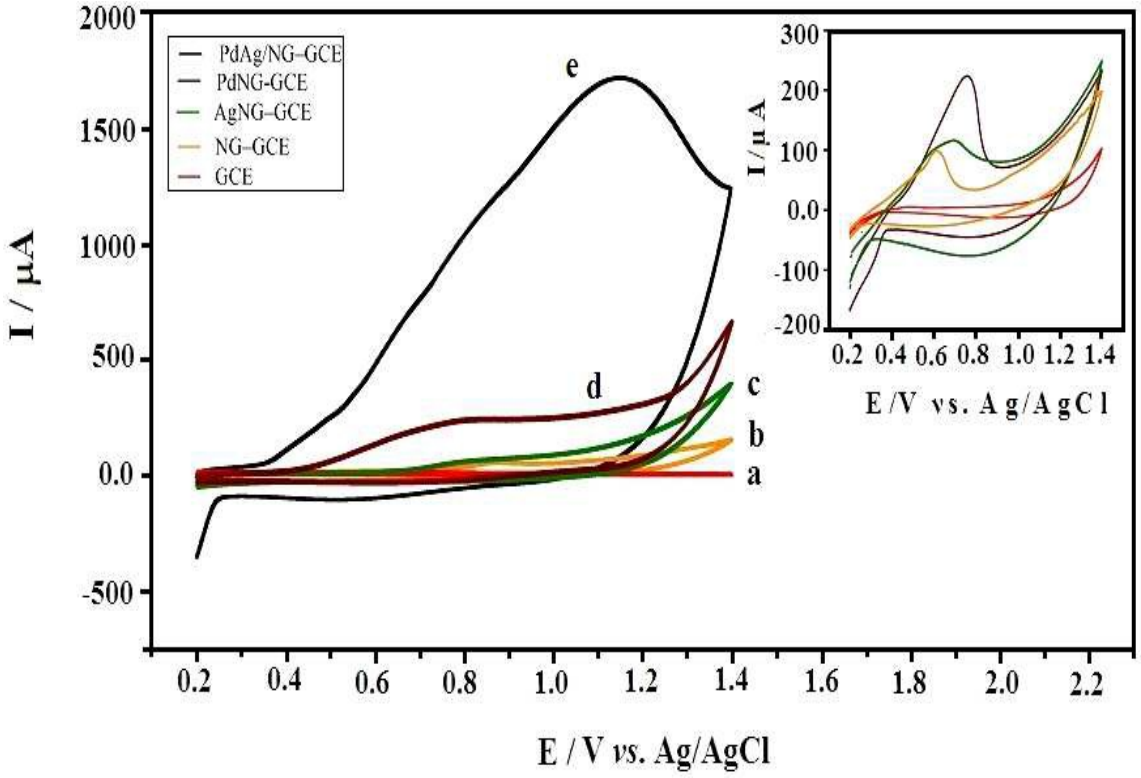

Fig. 6. CVs of 100 µM MTX in a 0.1 M phosphate buffer solution (pH 5.8) at 20 mV s^{-1} on (a) bare GCE, (b) NG–GCE, (c) Ag/NG–GCE, (d) Pd/NG–GCE, and (e) Pd_1Ag_1/NG–GCE.

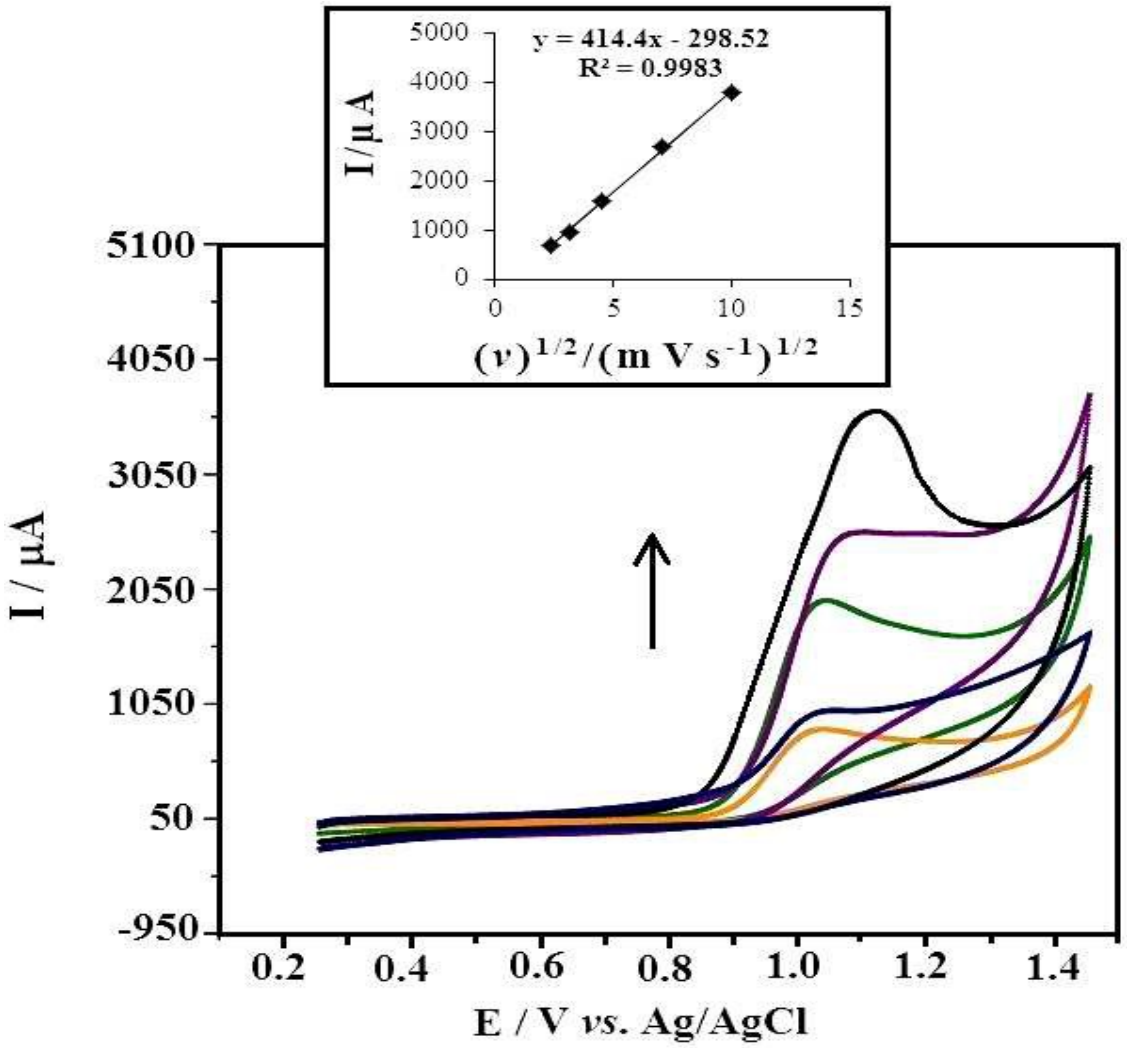

Fig. 7. CVs of 100 μM MTX in a 0.1 M phosphate buffer solution (pH 5.8) at the Pd_1Ag_1/NG–GCE at 5, 10, 20, 50 and 100 mVs^{-1}; Inset: plots of oxidation peak current versus the square root of the scan rate for MTX.

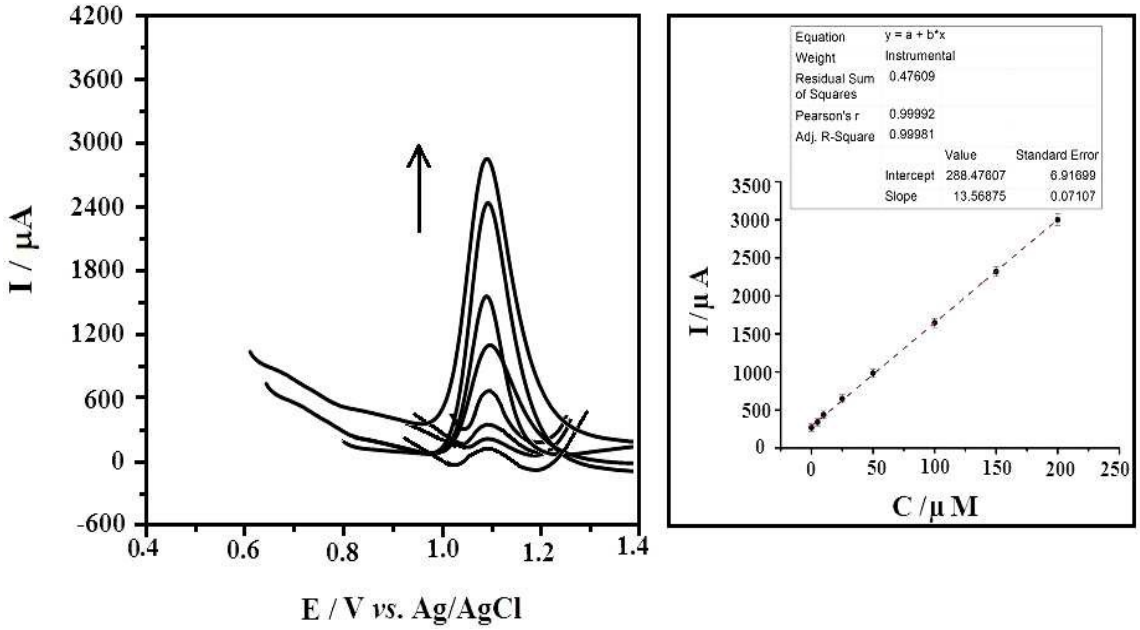

Fig. 8. Differential pulse voltammograms of 0.02, 5, 10, 25, 50, 100, 150 and 200 µM MTX in phosphate buffer (pH 5.8) at Pd_1Ag_1/NG–GCE.

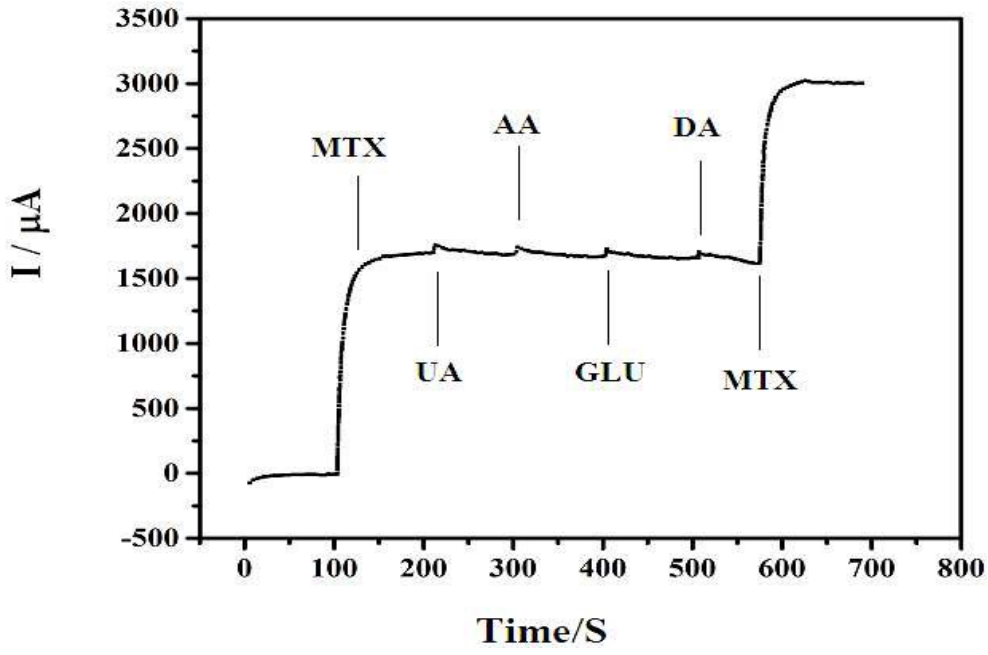

Fig. 9. Amperometric response of Pd_1Ag_1/NG–GCE upon the successive addition of 100 μM MTX, UA, AA, Glu and DA into 0.1 M phosphate buffer solution (pH 5.8) with an applied potential 1.1 V.

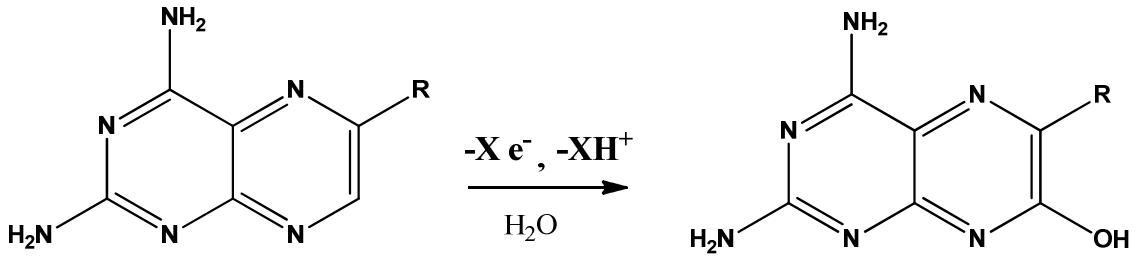

Scheme 1: Expected mechanism of MTX at Pd_1Ag_1/NG–GCE, (X= number of electron and proton, in equal numbers).

Table 1. Comparison of the performance of the modified electrodes from this study and previous reports for the analytical detection of MTX.

Electrode materials	Technique	Detection limit	Linear Range (μM)	Sensitivity (μA/μM)	Reference
DNA/SWCNT/Nafion/GCE	Square wave voltammogram (SWV)	8.0×10^{-3} μM	0.02–1.5	9.19	[55]
MWCNT/Screen-Printed Electrode (SPE)	SWV	0.1 μM	0.5–100	0.02302	[29]
Nano-Au/MWNTs-ZnO SPE	SWV	0.010 μM	0.020–1	0.3006	[56]
p-aminobenzene sulfonic acid/ quaternary MWCNTs/GCE	DPV	0.015 μM	0.1–8	0.5111	[54]
Cyclodextrin-graphene hybrid nanosheets /GCE	DPV	20 nM	0.1–1	67.8	[57]
Ag/NG–GCE	DPV	1.48 μM	5–150	0.771	
Pd/NG–GCE	DPV	1.07 μM	5-150	1.528	This work
Pd_1Ag_1/NG–GCE	DPV	1.32 nM	0.02–200	13.568	

Graphical Abstract:

The Pd_1Ag_1/NG–GCE is a promising platform for the highly sensitive electrochemical detection of MTX.